Materials Science & Engineering C 112 (2020) 110942

Contents lists available at ScienceDirect

Materials Science & Engineering C

journal homepage: www.elsevier.com/locate/msec

3D-printing of solvent exchange deposition modeling (SEDM) for a bilayered flexible skin substitute of poly (lactide-*co*-glycolide) with bioorthogonally engineered EGF

Daqian Gao[a], Zongliang Wang[b], Zhenxu Wu[b], Min Guo[b], Yu Wang[b,*], Zhenhua Gao[a,*], Peibiao Zhang[b,*], Yoshihiro Ito[c]

[a] The Ministry of Education Key Laboratory of Bio-based Material Science & Technology, College of Material Science and Engineering, Northeast Forestry University, Harbin 150040, PR China
[b] Key Laboratory of Polymer Ecomaterials, Changchun Institute of Applied Chemistry, Chinese Academy of Sciences, Changchun 130022, PR China
[c] Emergent Bioengineering Materials Research Team, RIKEN Center for Emergent Matter Science, 2-1 Hirosawa, Wako, Saitama 351-0198, Japan

ARTICLE INFO

Keywords:
Biodegradable polymer
3D printing
Solvent exchange
Tissue engineering
Growth factor
Skin regeneration

ABSTRACT

Biodegradable polyesters have been widely used as rigid biomedical apparatus because of high mechanical properties but few flexible implants. Herein, we report a flexible poly(lactide-*co*-glycolide) (PLGA) scaffold using a rapid *in situ* formation system based on phase separation by solvent exchange deposition modeling (SEDM), which was different from traditional 3D printing of fused deposition modeling (FDM). The FDM printed product was rigidity, its Young's modulus was approximate 2.6 times higher than that of SEDM printed sample. In addition, the thickness of the solidified ink would not shrink during the SEDM printing process, its surface had nano-/micro pores in favor of protein immobilization and cell adhesion. Then a flexible bilayered scaffold with nano-/microstructure was constructed combing SEDM with electrospinning technology for skin substitute, wherein the SEDM printed sample acted as a sub-layer for cell and tissue ingrowth, the densely packed electrospun nanofibers served as an upper-layer improving the sub-layer's tensile strength by 57.07% and preventing from bacteria as physical barrier. Ultimately, the bilayered scaffold immobilized epidermal growth factor (EGF) by a bioorthogonal approach was successfully applied to facilitate full-thickness wound healing of rats.

1. Introduction

Skin consists of epidermis, dermis, and hypodermis and is the largest organ of our body, accounting for 15% of an adult's body weight. The skin is the first barrier for defending against external invasion. Thus it is vital to promote fast and reliable skin regeneration after skin injury [1]. In the case of insufficient autograft resources and immunologic rejection of allografts and xenografts, skin substitutes developed through tissue engineering help in treating the patients with full-thickness injuries, especially those with large burn areas [2–4]. Although researchers have mimicked real skin in many aspects, including structure and functionality, there is still no perfect skin substitute because of the complex progress of wound healing (inflammation, granulation tissue formation, and remodeling) [1,5].

The structure and topography of a scaffold can affect cell behaviors such as adhesion, proliferation, and differentiation [6,7]. To simulate the extracellular matrix (ECM) of native tissue, biomimetic scaffolds with nano- and micro-structures have been developed [8]. In 2008, Park et al. first described nano-/microstructure prepared by a combination of electrospinning and FDM 3D printing [9–12]. The combination of the two processing methods had overcame the limitation of the nonwoven membranes prepared by traditional electrospinning and composed of densely packed nano fibers, which only allow cells to grow and migrate on their surface, not to infiltrate the inner part of the electrospun scaffolds [13]. The 3D printed scaffold can provide enough room for the growth of cells and granulation tissue [12,14]. But there is few report about how to construct a scaffold which is suitable for skin repair using this combining technology.

However, the stiffness of the materials can influence cell behaviors and should mimic that of native tissue [15,16]. The traditional FDM 3D printed rigid product is not suitable for skin substitutes. Additionally, the high temperature and viscosity of the FDM procedure might cause the thermal degradation of polymers. Hydrogel can be as the ink of direct-write 3D printed to prepare soft materials and mimic ECMs,

* Corresponding authors.
E-mail addresses: wydna@ciac.ac.cn (Y. Wang), gaozh1976@163.com (Z. Gao), zhangpb@ciac.ac.cn (P. Zhang).

https://doi.org/10.1016/j.msec.2020.110942
Received 4 January 2020; Received in revised form 6 March 2020; Accepted 7 April 2020
Available online 08 April 2020
0928-4931/

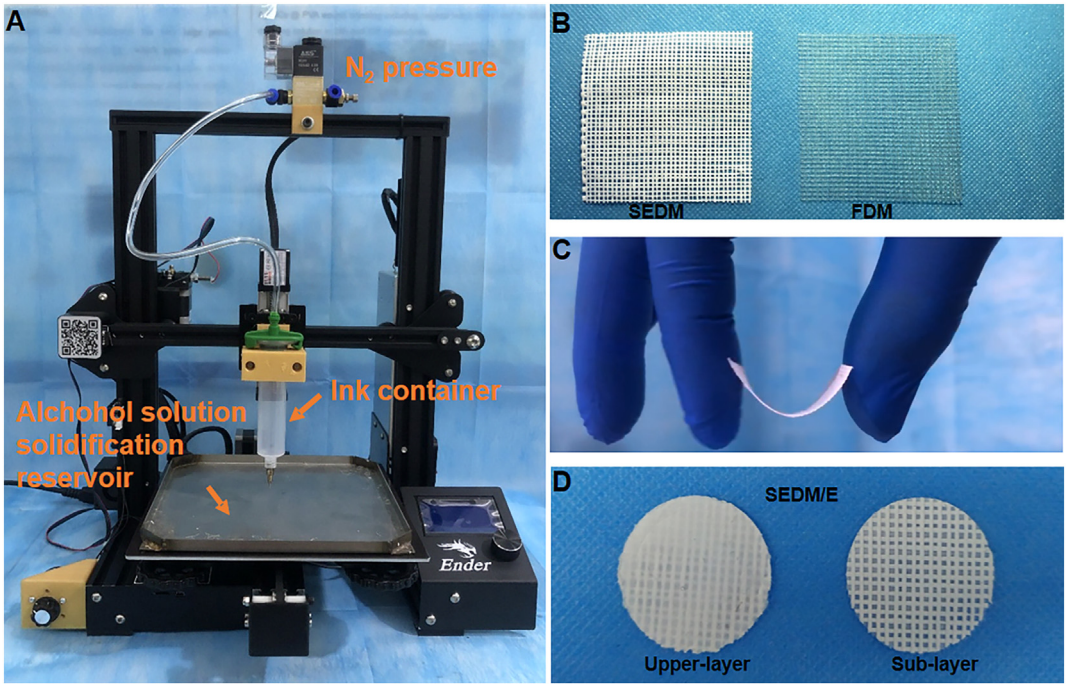

Fig. 1. The photographs of (A) the 3D printer for SEDM. (B) The SEDM sample (left) and FDM (right) scaffold. (C) The exhibition of elastic and flexible SEDM scaffold. (D) The upper-layer (left) and sub-layer (right) of the SEDM/E scaffold.

which may have poor strength [17]. Moreover, the hydrogel as printing ink should have temperature sensitivity, cross-linkable property or thixotropic behavior to maintain the shape of the ink and solidified in specific modeling environment. Cell laden hydrogels can be also printed by direct-write 3D printing. But cells in hydrogels can hardly secrete enough ECM and migrate easily to form cell-cell junctions [18]. Therefore, it is necessary to develop a simple 3D printing process to prepare flexible biodegradable polyesters with suitable strength and topography for cell and tissue growth.

Biodegradable polyesters thereof without biological activity are usually used in skin tissue engineering [1]. Hence, growth factors play an important role in this field. EGF can stimulate keratinocytes to proliferate and migrate promoting the wound healing [19,20]. Therefore, exogenous of EGF is necessary to accelerate wound healing while its activity should be maintained. Nevertheless, it has poor stability and rapid degradation in physiological environments leading to their low efficiency *in vivo*. If the applied dose is increased to maintain its activity, not only the cost but also the risk of cancer will increase [21,22]. Chemical binding growth factor may change the surface of a material and incur high costs, and physical adsorption is a low efficiency method [23]. To overcome these challenges, a suitable immobilization method should be chose to control its delivery.

Herein, we used a rapid *in situ* formation system based on solvent exchange deposition modeling (SEDM) 3D printing technology to fabricate a micro sized, flexible PLGA scaffold. In the process, PLGA of *N*-methyl pyrrolidone (NMP) solution was directly printed in ethanol solution at room temperature. The different flexibility and surface property between the SEDM and FDM scaffolds were investigated. To explore its applicability as a skin substitute, we combined SEDM with electrospinning technology constructing a flexible bilayered scaffold with nano-/micro structure. And EGF was immobilized on the scaffolds by recombinant DNA technology and tyrosinase treatment as our previous study described [24]. Fluorescence imaging method, Fourier transformation infrared spectroscopy (FT-IR) and X-ray photoelectron spectroscopy (XPS) was employed to evaluate the delivery process of EGF. *In vitro* and *in vivo* experiments were performed to evaluate the bilayered skin substitute.

2. Materials and methods

2.1. Synthesis of PLGA

PLGA (LA/GA = 75:25) with a mass average molecular weight of 150,000 was synthesized by the ring opening copolymerization of L-lactide and glycolide (Jinan Daigang Biomaterial Co., Ltd., China) using stannous octoate ($Sn(Oct)_2$ (Sigma Aldrich, USA) as catalyst [25].

2.2. SEDM 3D printing

A 3D printer (Bio-Fabrication Plus, Ubbiotech, China) for SEDM 3D printing as shown in Fig. 1A, and *SolidWorks* system were employed to prepare the sub-layer of the bilayered skin substitute. The synthetic PLGA was dissolved in N-Methyl pyrrolidone (NMP, Aladdin) with 40% (w/v) concentration as a printing ink. The printable property of PLGA dissolved in different solvent with the same concentration was also investigated as Fig. S3 shown. The inks were then solidified on a filter paper adsorbed ethanol solution. The applied pressure of nitrogen (N_2) on the PLGA solution and the nozzle extrusion speed were matched to achieve homogeneous linear fibers during the printing process. All printing parameters are listed in Table 1. The printing process is exhibited in Movie S1. Then the printed scaffolds were immersed into a 50% concentration ethanol solution for 48 h and vacuum freeze-dried to remove the organic solvent. The synthetic PLGA as above description was fed into a heating syringe for FDM 3D printing using 400 μm nozzle as control group [26]. Photographs of the scaffolds prepared by the SEDM and FDM are shown in Fig. 1B.

2.3. Fabrication of the bilayered scaffold

SEDM printed PLGA as sub-layer of the bilayered scaffold was fixed on the aluminum foil for receiving electrospun (E) PLGA nanofibers as upper-layer of the bilayered scaffold as shown in Fig. 1D. The synthesized PLGA was dissolved in hexafluoroisopropanol (HFIP) (Energy Chemical, China) at 10% (w/v) concentration as electrospun solution. The distance of the needle (20 gauge) tip to the collector was

Table 1
SEDM 3D printing parameters.

Parameter	Value
PLGA concentration (w/v)	40%
Extrusion pressure (MPa)	0.4
Nozzle diameter (μm)	400
Printing speed (mm/s)	72
Printing temperature (°C)	20
Ethanol bath dimension (cm^3)	18 × 18 × 1.2
Distance between nozzle to reservoir (mm)	2

maintained at 12 cm. 17 kV of voltage and 1 mL/h of flow rate was applied.

2.4. Preparation of DOPA-EGF and its immobilization on the scaffolds

3,4-Dihydroxyphenethylamine (DOPA) is a protein containing both amine and catechol functional groups secreted by mussels. It has excellent underwater adhesion property can bind on a wide spectrum of materials [27]. However, DOPA is a non-canonical amino acid, leading to it cannot be directly incorporated into a protein using conventional protein-engineering (recombinant DNA) techniques. Thus, DOPA was incorporated at the specific site of EGF protein using the bioorthogonal approach reported in our previous work without disturbing its tertiary structure, and its activity was maintained [24]. The EGF loading mechanism is shown as Fig. S1. Briefly, a pentapeptide tag (Tyr-Lys-Tyr-Lys-Tyr) residue was incorporated at the C-terminus of EGF by recombinant DNA technology. Then, the Tyr-Lys-Tyr-Lys-Tyr residues (500 ng/mL, 2 mL) were converted into DOPA-Lys-DOPA-Lys-DOPA by tyrosine hydroxylase (10 U/μL, 4 μL) (Sigma Aldrich, USA) in PBS solution with ascorbic acid (5 mg/mL, 1 mL) at pH 7.0–7.5 for 2 h in a 6-well plate (Corning Costar, US). Then the pH was adjusted to 8.0–8.5 and the samples were immersed into the solution for 16 h. The physical adsorption of EGF (500 ng/mL, 2 mL) was as a control group.

2.5. Characterization of the bilayered scaffolds

2.5.1. Scanning electron microscopy

The microstructures on the surface of the samples (SEDM, FDM, and SEDM /E) were observed by field emission scanning electron microscope (FE-SEM, Germany, Zeiss, Gemini 2). Their brittle-fractured surface, obtained through freezing in liquid N_2 and quickly breaking off, was also been observed. The applied voltage was 1 kV.

2.5.2. Nitrogen adsorption

The textural properties of the scaffolds prepared by SEDM and FDM 3D printing were confirmed by a nitrogen (N_2) adsorption/desorption experiment using a Quantachrome® ASiQwin™ instrument at 77.3 K. The Brunauer-Emmett-Teller (BET) equation was used to calculate the surface areas of the samples. The relative pressure (P/P_0) of the N_2 adsorption and desorption isotherms ranged from 0.1 to 1.0. The Barrett-Joyner-Halenda (BJH) model was employed to calculate the pore size distribution.

2.5.3. Bovine serum albumin (BSA) adsorption

To confirm the different surface property of SEDM and FDM, protein adsorption assay was performed. BSA (Bio Froxx, Germany) was chosen as a model protein because its isoelectric point at pH 4.6 is close to that of EGF. The scaffolds were cut into circular samples with 0.8 cm diameter and immersed in 100 μg/mL BSA solution at 37 °C under 150 rpm. The medium was collected at different time points from 5 min to 360 min for testing and then replaced by fresh PBS solution. The amounts of BSA adsorbed by the scaffolds were calculated through the decrease in BSA concentration of the medium using a BCA kit.

2.5.4. Mechanical properties

The tensile strength of the samples (E, SEDM, FDM, SEDM /E, and FDM/E) was tested by an Instron 5869 machine at a crosshead speed of 5 mm/min. The samples were cut into dumbbell shapes with dimensions of 15 × 2.5 × 0.29 mm^3. Five specimens of each group were tested.

2.5.5. Bacterial penetration

The samples (gauze, E, SEDM, and SEDM/E) were sterilized before test and cut into 10 mm diameter discs. *Escherichia coli* (*E. coli*) was cultured in lysogeny broth (LB) under 150 rpm shaking at 37 °C overnight. The bacteria suspension was diluted to 1 × 10^8 colony forming units (CFU)/mL, and 50 μl bacterial suspension was dropped onto the center of the samples. After the samples incubated at 37 °C for 24 h, the images of the bacterial growth was captured. Then the agar beneath the samples was cut into small pieces and immersed in 2 mL PBS with shaking by an ultrasonic cleaner to separate the cells from the agar. The OD value of the cell solution was recorded by a full wavelength microplate reader (Infinite M200, TECAN) [28]. Gauze was used as a positive control. Three duplicates of each group were performed.

2.6. Binding ability of DOPA-EGF

The spectra of the functional groups on the scaffolds were recorded by using FT-IR (Perkin Elmer 580B IR, USA) with a wavenumber range of 4000–500 cm^{-1} to confirm the SEDM/E scaffolds successfully binding of EGF (500 ng/mL). The chemical states of elements on the scaffolds were measured using XPS (Shimadzu/Kratos, Ltd., Japan).

A fluorescence imaging method was employed to investigate the binding efficiency of DOPA-EGF [29]. The scaffolds (E, SEDM and SEDM/E) were loaded with 500 μg/mL EGF using DOPA adhesion and physical absorption, respectively. The blank scaffolds were selected as control groups. The samples were washed using PBS 3 × 5 min, and then incubated with rabbit anti mouse EGF antibody (1:500 dilution) at 4 °C overnight. After washing 3 × 5 min with PBS, the scaffolds were incubated with a secondary Alexa Fluor 488 labelled goat-anti-rabbit IgG (1:500 dilution) antibody for 1 h at room temperature. The optical data were obtained using a fluorescence imaging device (CRi Maestro).

2.7. In vitro cell experiments

2.7.1. Cell culture

NIH 3T3 fibroblasts were cultured in medium composed of Dulbecco's modified Eagle's medium (DMEM, Gibco), 10% fetal bovine serum (Gibco), 10 mM HEPES (Sigma), 100 U/mL penicillin (Sigma) and 63 U/mL streptomycin (Sigma) at 37 °C and in a 5.0% CO_2 incubator. The medium was changed every 2 days.

2.7.2. Cell morphology and proliferation

The NIH 3 T3 cells were seeded on the scaffolds (E, SEDM, FDM, and SEDM/E with a diameter of 34 mm) at a density of 6 × 10^4/well in 6-well culture plates. For the SEDM/E group, the electrospun nanofibers were placed at the bottom of the culture plates and the SEDM printed scaffold was on the top. To observe the morphology of the cells and their distribution on the samples, live cells were stained with propidium iodide (PI)/calcein AM (Sigma, China) after incubation for 1 day and 3 days, respectively. Briefly, the samples were washed 3 times using PBS at regular time intervals. Then, the dual fluorescence PI and calcein were added and incubated for 10 min at 37 °C. Then, the scaffolds were washed several times with PBS, and observed using a fluorescence microscope (Nikon TU-2000, Japan). To further confirm the distribution of NIH3T3 cells on different samples at day 3, their visualized filamentous actin (F-actin) and nuclei (DAPI) were counterstained as previously described [30].

NIH 3 T3 cells were seeded on the scaffolds (diameter = 6 mm) at a density of 2 × 10^4/well in 96-well culture plates (Corning Costar, US)

and cultured for 1 and 3 days to evaluate cell proliferation using a cell count kit-8 (CCK-8, Dojindo, Japan). At each time point, 30 μL CCK-8 solution was added to the wells, and the samples were incubated for 2 h at 37 °C. Then, 100 μL of the reaction solution was transferred to a new 96-well plate. The full wavelength microplate reader was used to measure the samples' optical density (OD) values at 450 nm. Each group had four duplicates.

2.8. In vivo wound healing and histology analysis

The full-thickness excisional model was employed to evaluate the applicability of the bilayered scaffold as shown in Fig. 8C. Four male Sprague-Dawley (SD) rats in total with an average weight of 220–250 g were purchased from Jilin University. All the animal experiment procedures and protocols were in accordance with "The National Regulation of China for Care and Use of Laboratory Animals" promulgated by the National Science and Technology Commission of China, on November 14, 1988 as Decree No. 2. Protocol and approved by the Committee of Jilin University Institutional Animal Care and Use. The rats were anesthetized, and their dorsal surface was shaved and sterilized. Then, four full-thickness round wounds (diameter = 16 mm) were created on each rat. Then the blank scaffold and the scaffolds loaded with EGF and DOPA-EGF were implanted in the wound for 21 days to evaluate their ability of promoting skin regeneration. A silicone splint was sutured onto each wound margin to fix the scaffold. Post operation of the rats was maintained separately during the whole experiment. Each group had four duplicates.

The excisional wound changes were captured on days 0, 7, 14 and 21. The wound size was recorded at different time intervals. Wound closure rate was calculated using the following formula [31]:

$$\text{Wound closure rate } (\%) = (A_0 - A_t)/A_0 \times 100\%.$$

where A_0 represents the initial wound size, and A_t represents post operation of the wound size at day n = 7, 14 and 21. The silicone splints were removed as the wound began to scab.

Every two rats were sacrificed on days 14 and 21, respectively. The wound section tissues were collected, fixed in 4% formaldehyde PBS solution at 4 °C and embedded in paraffin. The sections were cut into 5 μm thicknesses for staining with hematoxylin−eosin (H&E) and Masson's trichrome as routine protocols.

2.9. Statistical analysis

All results were expressed as the means ± standard deviation (SD) of at least three duplicates. Variance analysis (ANOVA one-way, Origin 8.5) followed by Tukey method was used for the statistical analysis. A value of $P^* < 0.05$ was identified as statistically significant.

3. Results

3.1. Surface properties

SEM images (Fig. 2A–G) showed the microstructure of the surface and cross-section of the samples (SEDM, FDM, and SEDM/E). The surface of the SEDM sample (Fig. 2A) had pores with different sizes and rough surface due to the solvent exchange, which might be better for cell adhesion and growth. In contrast, the surface of the FDM group (Fig. 2B) had no pores and was smooth. Electrospun nanofibers stacked on the SEDM fibers to construct a bilayered structure with nano- and microstructures (Fig. 2C–D). The sub-layer (Fig. 2C) was micro sized SEDM 3D printed strut, and the upper-layer (Fig. 2D) was nanofibers. The brittle-fractured surface of the SEDM group (Fig. 2E) was also rough and had pores. In contrast, the surface was smooth for the FDM group (Fig. 2F). Observation of the brittle-fractured surface of the SEDM/E group (Fig. 2G) confirmed that the electrospun meshes were stacked tightly on the SEDM scaffolds.

However, some micro- (pore diameter < 2 nm) or mesopores (2 nm < pore diameter < 10 nm) might not be observed by SEM, because they might be covered by some macropores (pore diameter > 10 nm) [32]. Thus, we employed N_2 adsorption to detect the micro- or mesopores on the surface of SEDM. The N_2 adsorption/desorption isotherms of the scaffolds (SEDM and FDM) are shown in Fig. 2H. The curve of the SEDM group can be identified as a type V isotherm, and its hysteresis loop belongs to type H3 [33,34]. The N_2 adsorption results of the SEDM scaffold indicated that its surface had also micro- and mesopores. The average pore diameter, BET surface area and pore volume are exhibited in Table 2. The curve of the FDM group showed type II isotherms (Fig. 2H), indicating its surface was smooth in accord with the SEM results (Fig. 2B).

The time-adsorption curves of the model protein (BSA) on SEDM and FDM at pH 7.4 were shown in Fig. 2I. After soaking in BSA for 30 min, they both reached equilibrium adsorption. The SEDM group had adsorbed 134.98 μg of BSA, which was higher than that (109.19 μg) of the FDM group. This further proved that the surface of SEDM scaffold with nano-/micro pores was beneficial for protein adsorption.

3.2. Mechanical properties

The tensile strength of the electrospun nanofibers was 3.80 MPa about 2.30 and 3.53 times higher than that 1.65 (MPa) of the SEDM groups and that (1.08 MPa) of FDM groups (Fig. 3A), respectively. After electrospun nanofibers stacking on the 3D printed scaffolds, the strength of the SEDM and FDM groups were reinforced by 57.07% and 106.51% and reached to 2.59 MPa and 2.22 MPa, respectively. The stress−strain curve (Fig. 3B) revealed that the SEDM scaffolds exhibited the ductile fracture at the stress yield point. And the curves of the FDM samples exhibited brittle fracture, indicating that the SEDM scaffold exhibited better elasticity and flexibility than the FDM group. The FDM sample showed much higher Young's modulus (174.50 MPa) than that (66.10 MPa) of the SEDM sample (Fig. 3C), further revealing its rigidity and hardly deformation. The elastic and flexible properties of the SEDM scaffold were also shown in Fig. 1C and Movie S2. Furthermore, the flexible of SEDM printed sample was influenced by the printed layers as Fig. S4. When 8 or more layers were printed, the yield platform of the stress-strain curve deceased indicating the toughness reduced. The warpage also occurred with the printed layers increased.

3.3. Bacterial penetration

There was enough space for cell and tissue ingrowth between the SEDM 3D printed strut, it also easily invaded by bacteria. However, the densely packed electrospun nanofibers as physical barrier can prevent from the bacteria. As shown in Fig. 4, the OD value of the SEDM group was highest at 0.95, the gauze followed at 0.59. And the bacterial cells surrounded the SEDM and gauze, indicating they can easily penetrate the micro sized structure. The E and SEDM/E groups had lower OD value at 0.26 and 0.12, respectively, demonstrating the bacteria can hardly penetrate the electrospun nanofibers.

3.4. Growth factor binding assay

Fig. 5A showed the FT-IR spectra results. For EGF and DOPA-EGF group, the band from 3600–3000 cm^{-1} and 1680 to 1590 cm^{-1} was attribute to N−H stretching vibration, C=O bending and C−N stretching vibrations of amide groups [35–37], which belonged to amide group of protein, indicating that EGF was successfully immobilized on the surface of the samples. Moreover, the XPS results showed EGF group (Fig. 5B) had a new peak of N1s at 400 eV, and the DOPA-EGF group had a double peak of N1s at 399 eV and 403 eV due to the incorporation of the amino group of dopamine. The quantitative analysis results of XPS data were listed in Table 3. The surface of the DOPA-EGF group had more N element (4.05%) than the EGF group

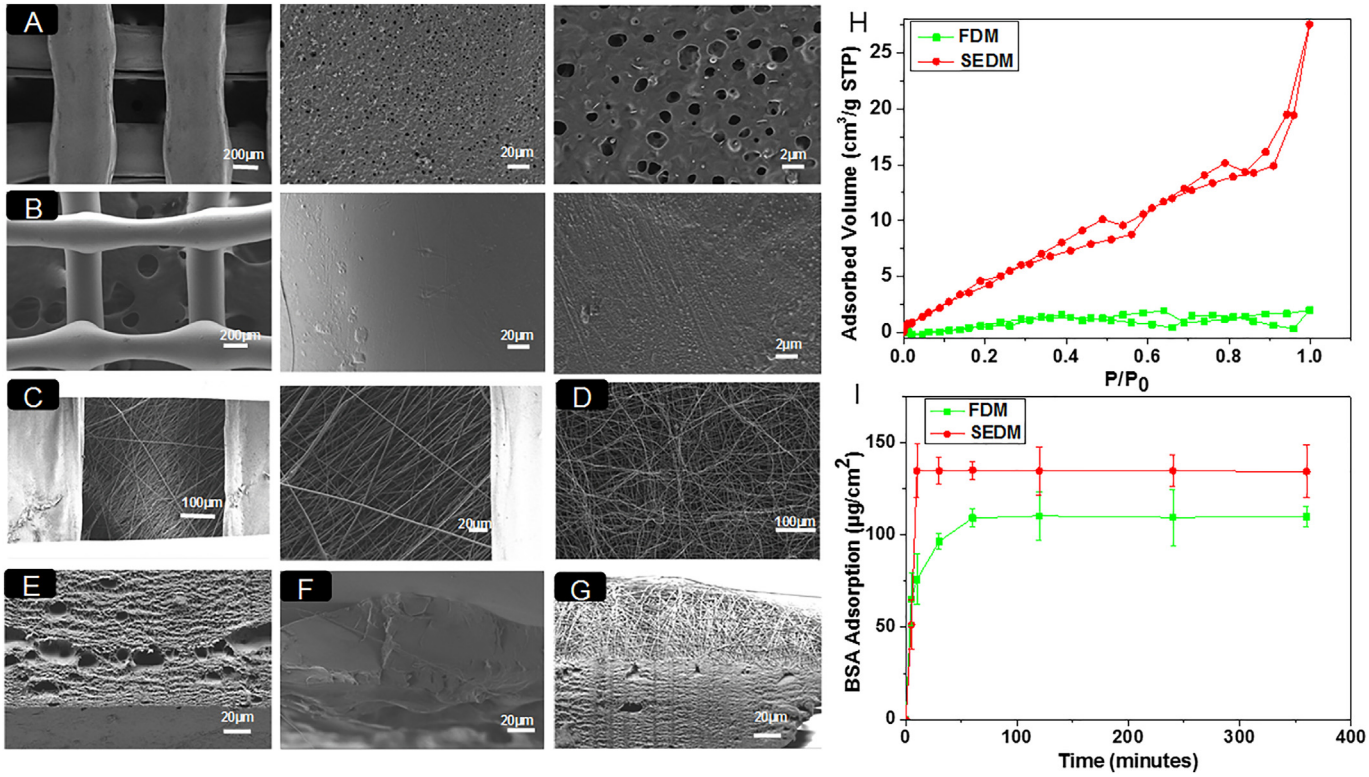

Fig. 2. SEM images: the surface of (A) the SEDM, (B) FDM scaffolds, (C) sub-layer and (D) upper-layer of the SEDM/E scaffold. Fractured surface of (E) the SEDM, (F) FDM and (G) the SEDM/E scaffolds. (H) N_2 adsorption/desorption isotherms and (I) BSA adsorption rate of the SEDM and FDM groups.

Table 2
The surface area S_{BET}, pore volume V_p and BJH adsorption average pore diameter.

	S_{BET} (m^2/g)	V_p (cm^3/g)	D_P (nm)
SEDM	25.30	0.04	5.00
FDM	0.00	0.01	0.00

(2.93%), indicating that the amount of DOPA-EGF was higher than physically adsorbed EGF, which was also proved by static water contact angle result in Fig. S6.

We had further quantified the immobilized amounts of EGF and DOPA-EGF groups on the samples using the immunofluorescence assay (Fig. 5C and D). The results showed that the fluorescence signal of the DOPA-EGF group was stronger than that of the EGF group, indicating that binding amount of DOPA-EGF group was higher than that of EGF group due to the excellent adhesion properties of the catechol of DOPA

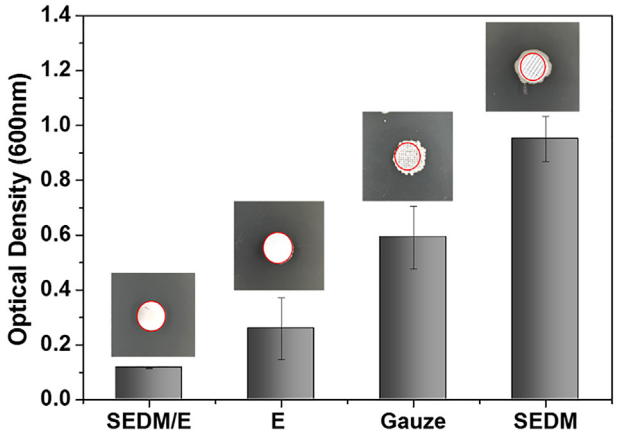

Fig. 4. Bacterial penetration of the SEDM/E, E, gauze and SEDM scaffolds.

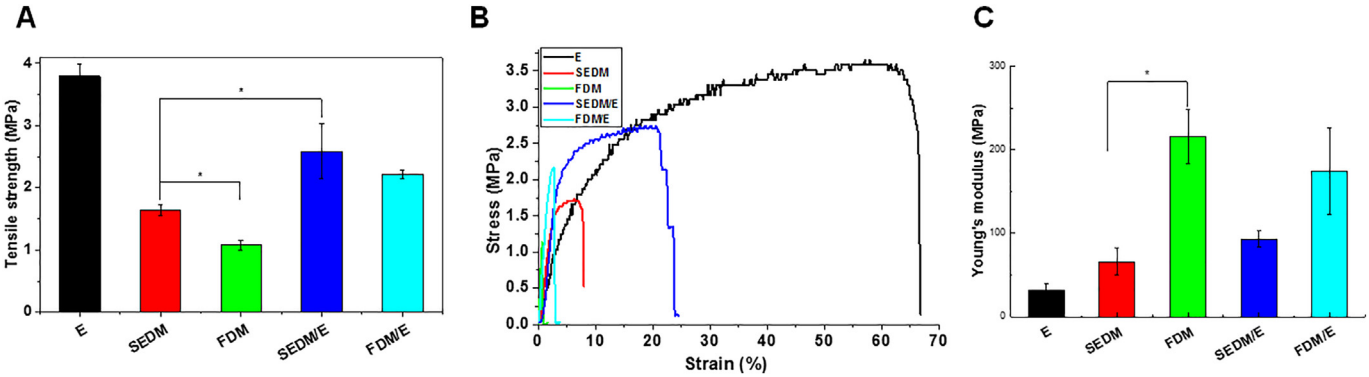

Fig. 3. (A) Tensile strength, (B) stress−strain curves and (C) Young's modulus of the E, SEDM, FDM, SEDM/E and FDM/E scaffolds. (* indicates significant differences, $p < 0.05$, $n = 5$).

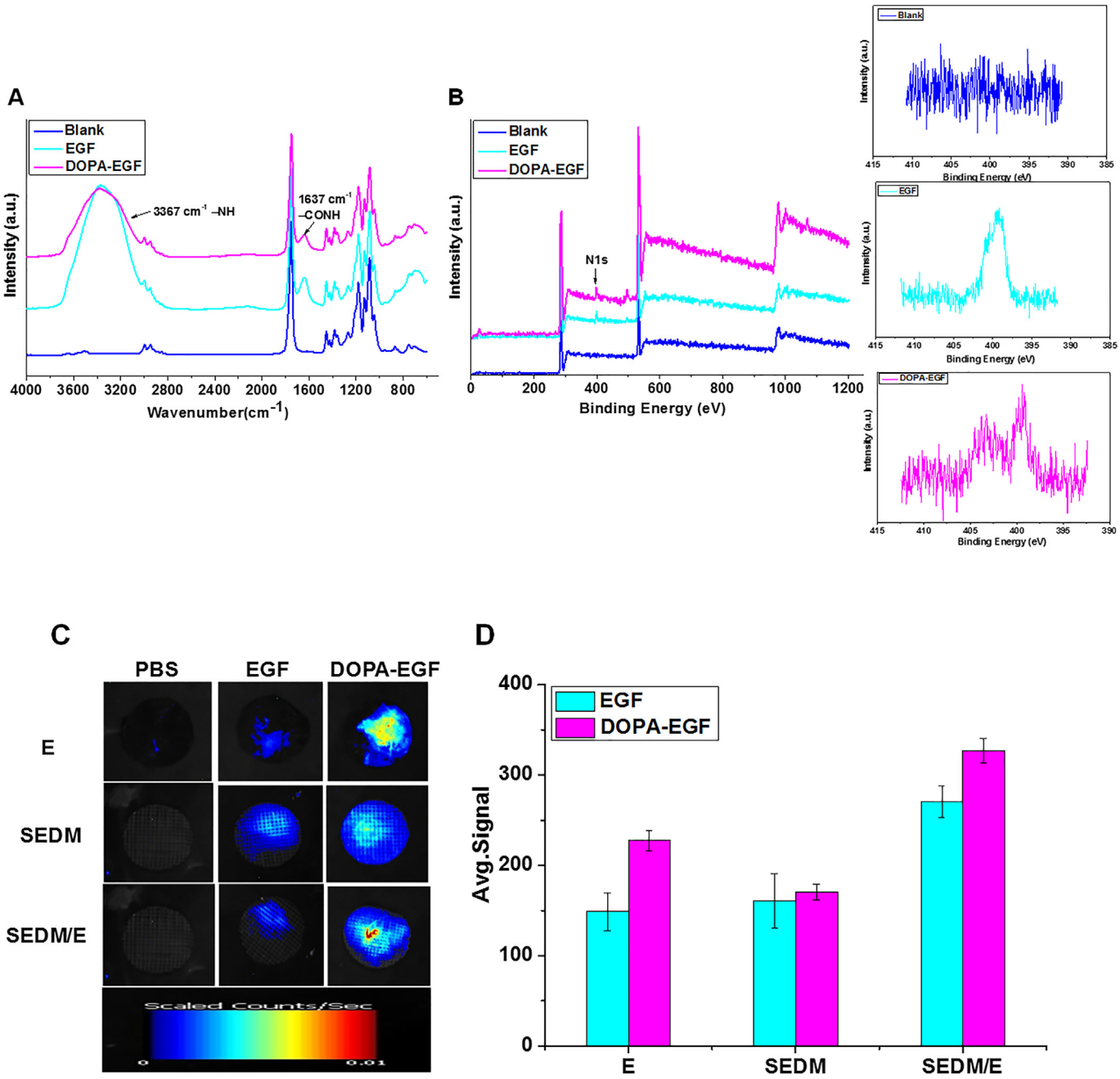

Fig. 5. Evaluation of EGF immobilization: (A) FT-IR, (B) XPS of the SEDM/E scaffold loaded with EGF using physical adsorption and DOPA adhesion, (C) immunofluorescence images and (D) average fluorescence signal of the E, SEDM and SEDM/E scaffolds loaded with EGF by physical adsorption and DOPA adhesion. (The average fluorescence signal of blank groups cannot be detected).

Table 3
Elemental mole percent calculated from XPS Spectra for the surface of SEDM/E scaffolds.

	C (%)	O (%)	N (%)	S (%)
Blank	76.02	23.98	0	0
EGF	85.55	11.53	2.93	0
DOPA-EGF	64.75	28.01	4.05	0.19

through quinone covalent coupling to the materials.

3.5. Cell adhesion and proliferation

We chose NIH 3 T3 fibroblasts in this study due to the fibroblasts of the substantial presence in the granulation tissue during wound healing [38]. The morphology and distribution of NIH 3 T3 fibroblasts on different scaffolds were exhibited as the results of the live cell staining (Fig. 6A), F-actin and nuclei staining (Fig. 6B). The cells only grown on the surface of electrospun nanofibers without into their inner parts. For the SEDM and FDM groups, the cells only grew on the strut of the scaffolds but could not migrate from one strut to another due to the large gap. The amounts of the cells on the SEDM/E scaffolds were most and their distribution was more reasonable because of the cells adhesion and growth on both nanofibers and micro sized 3D printed strut. The nano fibrous membranes acted as an upper-layer substrate for cell adhesion and migration, and the SEDM scaffolds provided enough room for cell ingrowth. The scaffold architecture containing nano-, micro-, and macroscales are more suitable for tissue engineering [7,12,39].

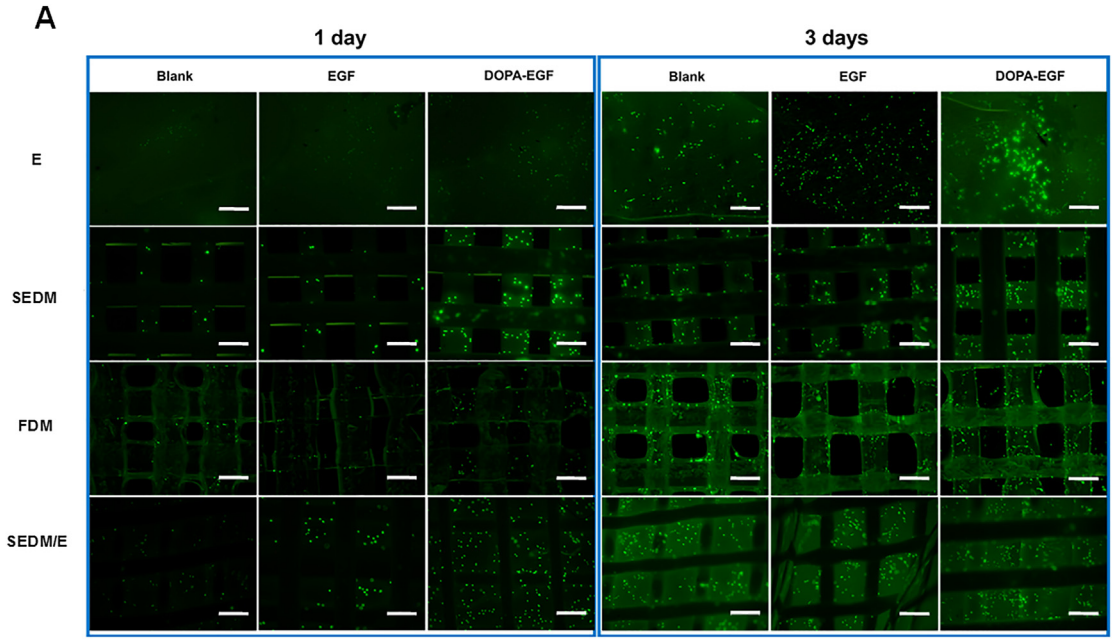

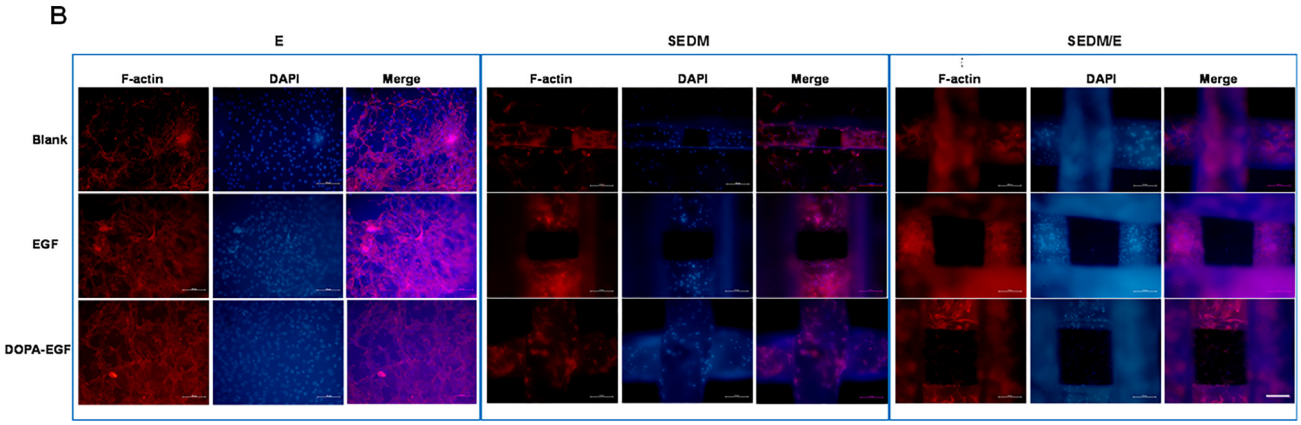

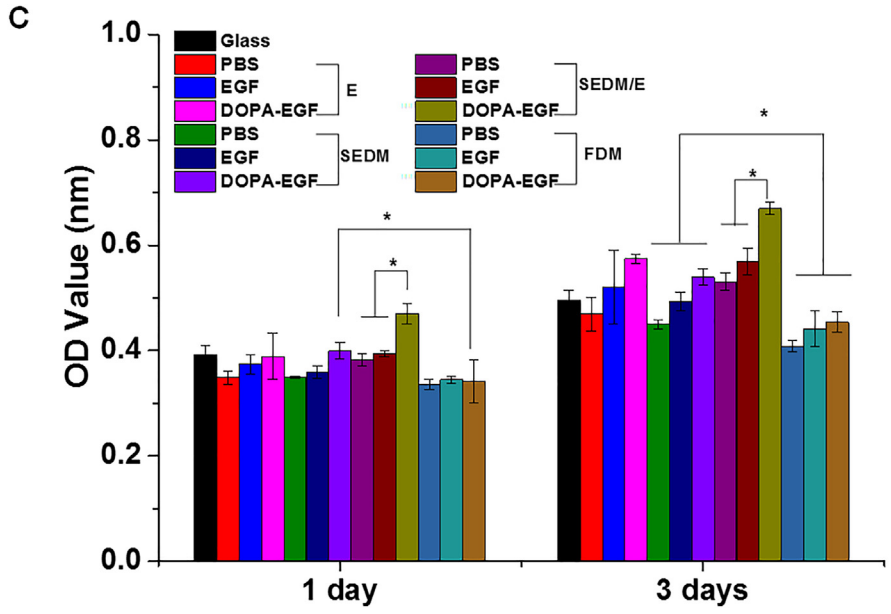

(caption on next page)

Fig. 6. (A) Live cell staining images: The morphology and distribution of the NIH3T3 fibroblast cells on the E, SEDM, FDM, SEDM/E scaffolds loaded with EGF using physical adsorption and DOPA adhesion at day 1 and 3. Scale bar = 500 μm. (B) F-actin (red) and nuclei (blue) images of the NIH3T3 fibroblast cells on the E, SEDM, SEDM/E scaffolds at day 3. Scale bar = 200 μm. (C) NIH3T3 cells proliferation on the E, SEDM, FDM, SEDM/E scaffolds at day 1 and 3. (* indicates significant differences, $p < 0.05$, $n = 4$). (For interpretation of the references to color in this figure legend, the reader is referred to the web version of this article.)

Furthermore, the DOPA-EGF group had the most live cells in each processing method.

NIH 3 T3 cell proliferation was shown in Fig. 6C. For the same protein loading method, the cell proliferation at day 1 and 3 of the SEDM group was higher than that of FDM group, indicating the rough surface of SEDM printed scaffold was beneficial for cell growth than the smooth surface of FDM printed scaffold. The SEDM/E samples with nano-/micro structure had the highest cell proliferation, indicating this complicated topography promoted the cell proliferation, which was in accordance with the results of Fig. 6A and B. Moreover, the DOPA-EGF group in each processing method had higher cell proliferation than EGF and PBS groups due to the high immobilization of EGF on the samples, which was further confirmed by the relative gene expression (as shown in Fig. S7).

3.6. In vivo wound healing assessment and histology analysis

The observation of wound closure progress, the calculation of wound closure rates and the full-thickness excisional model were shown in Fig. 7A–C. The wound closure rate at day 7 of the DOPA-EGF group (40.63%) was faster than that of control (31.25%), blank (33.50%) and EGF (37.50%) groups. The SEDM/E scaffolds loaded with DOPA-EGF exhibited the strongest ability to promote wound healing; their closure rate reached 84.38% at day 14 and 98.88% at day 21. The closure rate of EGF group followed with 75.00% and 89.63% at days 14 and 21, respectively. Their closure rates were both much higher than those of the blank and control groups.

The H&E and Masson's trichrome results were shown in Fig. 8A–B. The H&E staining images can show the inflammatory response, granulation tissue and re-epithelialization of the wound histology sections. Healthy granulation formation can transport nutrients and growth factor during epidermal regeneration, which is important for wound healing. Then the granulation was gradually replaced by collagen fibers during the wound healing [40]. Hair follicles and thick epidermis can be observed in the DOPA-EGF group at day 14 as H&E staining images shown (Fig. 8A). Finally, well-developed homogeneous and continuous dermis of the DOPA-EGF group can be seen at day 21 (as indicated by the dark arrow), indicating that re-epithelialization of the DOPA-EGF was better than other groups. Collagen deposition in the dermis of the wound tissue was observed (Fig. 8B). At day 14, the DOPA-EGF group exhibited the highest collagen deposition, indicated by blue color intensity (where the blue is deeper, the collagen deposition is higher). The collagen deposition of the DOPA-EGF group exhibited dense packing and a regular orientation at day 21, unlike other groups' loose packing and irregular arrangement. These results revealed that the SEDM/E scaffolds binding DOPA-EGF could effectively promote wound healing.

4. Discussion

Biodegradable polyesters, such as PLGA, with high molecular usually were subjected to FDM 3D printing for high mechanical properties of medical application. The major aim of this work was to develop a 3D printing process for preparing elastic and flexible PLGA. The SEM, N_2 adsorption results and BSA adsorption analysis (Fig. 2A, B, H and I) revealed different surface properties between SEDM and FDM groups. The same nozzle was used in SEDM and FDM process, but the shrinkage happened during FDM printing process as Fig. 2B shown, because the sharp melt-to-solid transition [16]. However, the solidified ink did not shrink during the SEDM process due to the suitable solvent exchange

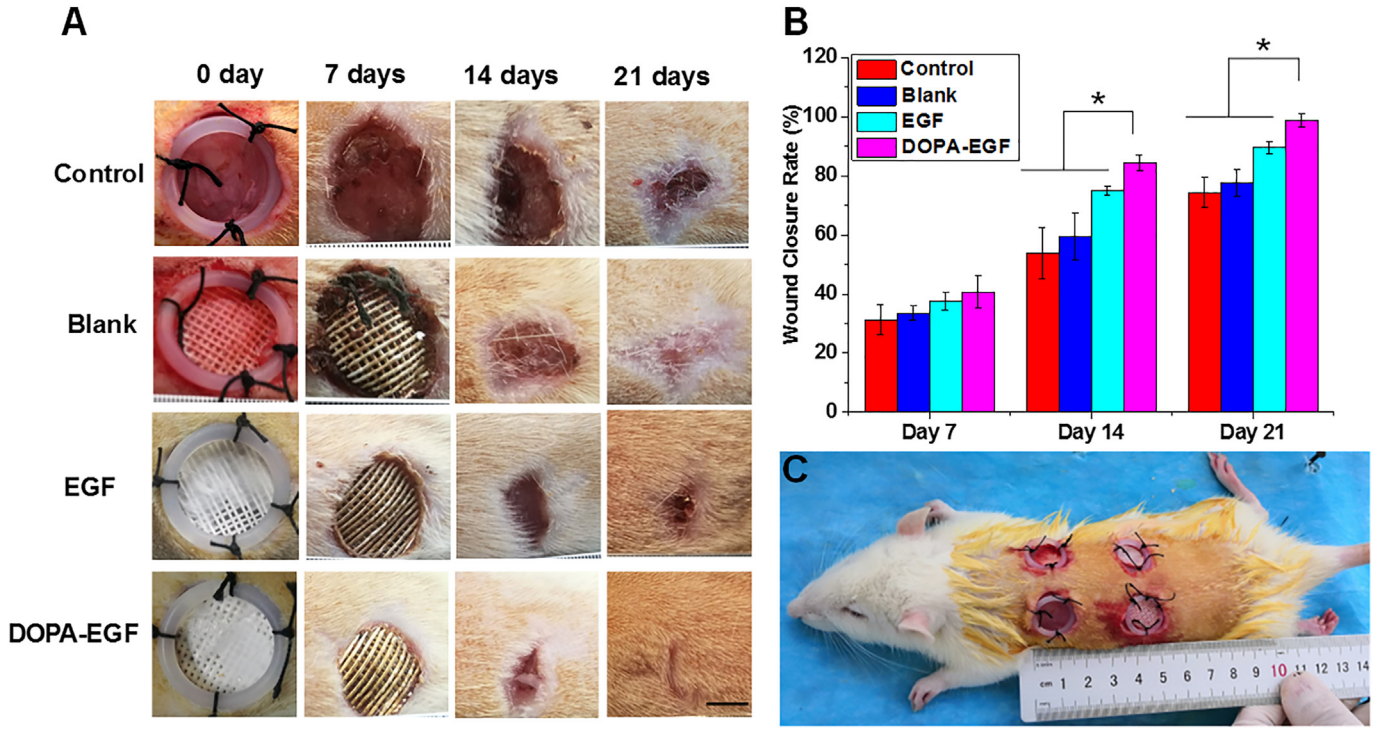

Fig. 7. (A) Observation of wound closure (B) wound closure rate treated with nothing (control), the blank SEDM/E scaffold, and the SEDM/E scaffold loaded with EGF using physical adsorption and DOPA adhesion at day 7, 14, and 21. (C) Photographs of the excisional wound model. (* indicates significant differences between Blank, EGF and DOPA-EGF groups at days 14 and 21, $p < .05$, $n = 5$, scale bar = 5 mm).

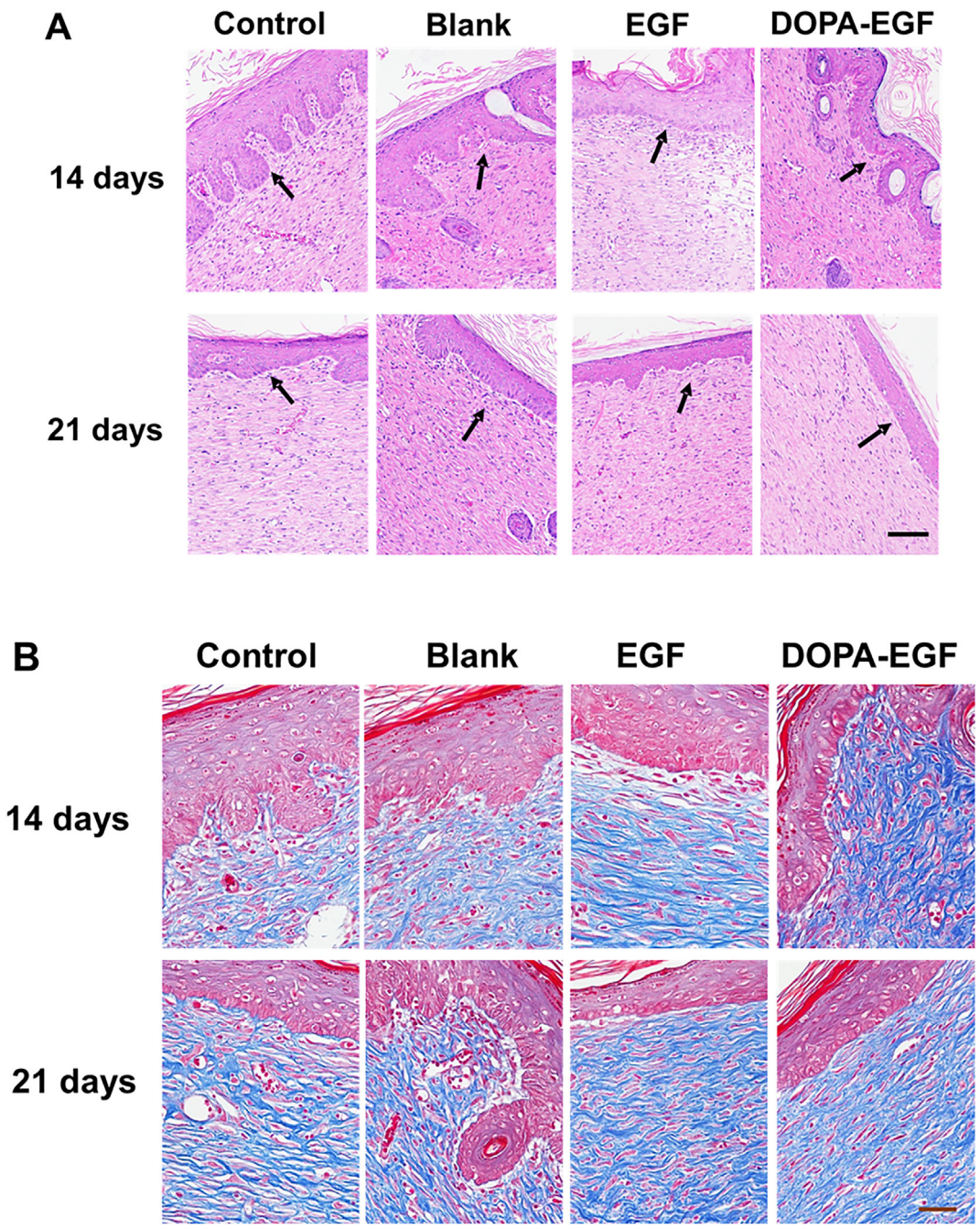

Fig. 8. Images of (A) H&E staining (magnification: 200×), scale bar = 100 μm, and (B) Masson's trichrome staining (magnification: 400×), scale bar = 50 μm (brown), at day 14 and 21 post-operation. (For interpretation of the references to color in this figure legend, the reader is referred to the web version of this article.)

time. If we directly printed the ink into a coagulation reservoir instead of on a filter paper, the printed strut may still seriously shrink as literature reported [41]. The tensile strength results (Fig. 3A–C) revealed that the SEDM sample exhibited toughness and had higher tensile strength than rigid and brittle FDM sample due to the high temperature that may lead to thermal degradation of partial PLGA in the heating syringe as DSC results shown (Fig. S5).

Nanostructure can enhance initial cell attachment and cell proliferation [10,42]. Therefore, a bilayered scaffold was constructed combining SEDM 3D printing with electrospinning to explore its potential as skin substitute. The micro-sized pore between the SEDM 3D printed strut can contribute to cell proliferation and tissue regeneration [28,43,44]. This nano-/microstructure make their respective advantages complementary to each other. The tensile strength of SEDM sample can be enhanced by electrospun nanofibers (Fig. 3A–B). The nanofibers can be also used as a physical barrier to prevent from bacteria (Fig. 4).

A EGF derivative was prepared by a green and high efficient approach as our previous study described [24]. The FT-IR (Fig. 5A) results showed the successful immobilization of EGF. The XPS (Fig. 5B), fluorescence imaging (Fig. 5C–D) and water contact angle (Fig. S6) results revealed the excellent binding property of DOPA-EGF [45].

Live cells staining (Fig. 6A) and fluorescent staining (Fig. 6B) results revealed the NIH3T3 cell spread on the nanofibers and micro sized strut of the bilayered scaffold, whose topography was more beneficial to cell proliferation and ingrowth. Cell proliferation plays an important role in the wound healing process [46], its result (Fig. 6C) indicated that the SEDM group with rough surface was more suitable for cell growth than

the smooth surface of the FDM group. Cell proliferation of DOPA-EGF group was the best due to the high binding amounts of EGF.

In vivo experiment was used to further verify the applicability of the bilayered scaffolds on wound healing. The SEDM/E samples loaded with DOPA-EGF can effectively promote full-thickness excisional wound healing (Figs. 7–8). But 16 mm is a large wound for the rat. Marques et al. [47] created a 12 mm diameter full-thickness excision, while there was still an obvious scab (approximate 5 mm) in their control group at day 21. Fathima et al. [48] used a 2 cm^2 × 2 cm^2 of excisional wound model, the control group also not closed after 16 days. The normal healing period should be during 18–20 days. However, Qu et al. [5] create only an 8 mm diameter of full-thickness round wounds, their control group has not still totally healed at day 21. Because they use an excisional wound splinting model [49] in that a splinting ring tightly adheres to the skin around the wound, preventing wound closure caused by skin contraction. Similarly, we also used a splint to fix the scaffold on the wound, which may influence the wound healing speed of the rat, although we took them out at day 3 when the wound had begun to scab. This is the reason that we can see the scar at day 21 in the four experiment groups. Furthermore, PLGA is a synthetic biocompatible polyester, but it still can cause some inflammatory response of the rat during its degradation period, which may also effect the wound closure rate of the rat.

Therefore, the degradation property of the bilayered scaffold during the wound healing also need be further investigated in the future work. It may be a solution to decrease inflammatory response *in vivo* that alginate or other hydrogel was coated on the synthetic polymer.

5. Conclusions

In this article, we present a novel 3D printing method, which was easy to handle, to prepare a flexible PLGA scaffold at room temperature. The results of tensile strength indicated that the sample prepared by SEDM method exhibited toughness rather than rigid like the sample prepared by FDM. The surface of SEDM scaffold was rough and had pores in favor of protein adsorption and cell growth. Notably, a bilayered scaffold with nano-/micro structure prepared by SEDM 3D printing and electrospinning technology and immobilized DOPA-EGF by the bioorthogonal approaches have effectively promoted the wound healing of the rats. It can be suggested that this bilayered scaffold is a potential candidate for wound care applications.

Supplementary data to this article can be found online at https://doi.org/10.1016/j.msec.2020.110942.

Declaration of competing interest

The authors declare that they have no known competing financial interests or personal relationships that could have appeared to influence the work reported in this paper.

Acknowledgements

This work was supported by the Fundamental Research Funds for the Central Universities of China (2572018AB17), the National Natural Science Foundation of China (Projects 51673186).

References

[1] S. Vijayavenkataraman, W.F. Lu, J.Y.H. Fuh, 3D bioprinting of skin: a state-of-the-art review on modelling, materials, and processes, Biofabrication 8 (2016) 032001, , https://doi.org/10.1088/1758-5090/8/3/032001.

[2] M.W.J. Ferguson, Bioengineering skin using mechanisms of regeneration and repair, Biomaterials 28 (2007) 5100–5113, https://doi.org/10.1016/j.biomaterials.2007.07.031.

[3] S.G. Kumbar, S.P. Nukavarapu, R. James, L.S. Nair, C.T. Laurencin, Electrospun poly(lactic acid—glycolic acid) scaffolds for skin tissue engineering, Biomaterials 29 (2008) 4100–4107, https://doi.org/10.1016/j.biomaterials.2008.06.028.

[4] B.K. Sun, S. Zurab, P.A. Khavari, Advances in skin grafting and treatment of cutaneous wounds, Science 346 (2014) 941–945, https://doi.org/10.1126/science.1253836.

[5] Y. Qu, C. Cao, Q. Wu, A. Huang, Y. Song, H. Li, Y. Zuo, C. Zhu, J. Li, Y. Man, The dual-delivery of KGF and bFGF by collagen membrane to promote skin wound healing, J. Tissue Eng. Regen. Med. 12 (2018) 1508–1518, https://doi.org/10.1002/term.2691.

[6] M. Kim, W. Kim, G. Kim, Topologically micro-patterned collagen and PCL struts fabricated using the PVA fibrillation/leaching process to develop efficiently engineered skeletal muscle tissue, ACS Appl. Mater. Interfaces 9 (2017) 43459–43469, https://doi.org/10.1021/acsami.7b14192.

[7] J.I. Kim, C.S. Kim, Nanoscale resolution 3D printing with pin-modified electrified inkjets for tailorable nano/macrohybrid constructs for tissue engineering, ACS Appl. Mater. Interfaces 10 (2018) 12390–12405, https://doi.org/10.1021/acsami.7b19182.

[8] H. Ding, M. Zhong, H. Wu, S. Park, J.W. Mohin, L. Klosterman, Z. Yang, H. Yang, K. Matyjaszewski, C.J. Bettinger, Elastomeric conducting polyaniline formed through topological control of molecular templates, ACS Nano 10 (2016) 5991–5998, https://doi.org/10.1021/acsnano.6b01520.

[9] S.H. Park, T.G. Kim, H.C. Kim, D.Y. Yang, T.G. Park, Development of dual scale scaffolds via direct polymer melt deposition and electrospinning for applications in tissue regeneration, Acta Biomater. 4 (2008) 1198–1207, https://doi.org/10.1016/j.actbio.2008.03.019.

[10] G.H. Kim, J.G. Son, S. Park, W.D. Kim, Hybrid process for fabricating 3D hierarchical scaffolds combining rapid prototyping and electrospinning, Macromol. Rapid Commun. 29 (2010) 1577–1581, https://doi.org/10.1002/marc.200800277.

[11] L. Moroni, J.B. De Wijn, C.A. Van Blitterswijk, Integrating novel technologies to fabricate smart scaffolds, J. Biomater. Sci. Polym. Ed. 19 (2008) 543–572, https://doi.org/10.1163/156856208784089571.

[12] P.D. Dalton, C. Vaquette, B.L. Farrugia, T.R. Dargaville, T.D. Brown, D.W. Hutmacher, Electrospinning and additive manufacturing: converging technologies, Biomater. Sci. 1 (2013) 171–185, https://doi.org/10.1039/C2BM00039C.

[13] H. Li, Y. Xu, X. He, C. Jiang, Electrospun membranes: control of the structure and structure related applications in tissue regeneration and drug delivery, J. Mater. Chem. B 2 (2014) 5492–5510, https://doi.org/10.1039/C4TB00913D.

[14] C. Vaquette, W. Fan, Y. Xiao, S. Hamlet, D.W. Hutmacher, S. Ivanovski, A biphasic scaffold design combined with cell sheet technology for simultaneous regeneration of alveolar bone/periodontal ligament complex, Biomaterials 33 (2012) 5560–5573, https://doi.org/10.1016/j.biomaterials.2012.04.038.

[15] T.H. Kim, B.A. Dan, S.H. Oh, K.K. Min, H.H. Song, H.L. Jin, Creating stiffness gradient polyvinyl alcohol hydrogel using a simple gradual freezing–thawing method to investigate stem cell differentiation behaviors, Biomaterials 40 (2014) 51–60, https://doi.org/10.1016/j.biomaterials.2014.11.017.

[16] M. Guvendiren, J. Molde, R.M. Soares, J. Kohn, Designing biomaterials for 3D printing, ACS Biomater. Sci. Eng. 2 (2016) 1679–1693, https://doi.org/10.1021/acsbiomaterials.6b00121.

[17] G. Della Giustina, A. Gandin, L. Brigo, T. Panciera, S. Giulitti, P. Sgarbossa, D. D'Alessandro, L. Trombi, S. Danti, G. Brusatin, Polysaccharide hydrogels for multiscale 3D printing of pullulan scaffolds, Mater. Des. 165 (2019) 107566, https://doi.org/10.1016/j.matdes.2018.107566.

[18] J.W. Nichol, A. Khademhosseini, Modular tissue engineering: engineering biological tissues from the bottom up, Soft Matter 5 (2009) 1312–1319, https://doi.org/10.1039/B814285H.

[19] S.M. Choi, K.M. Lee, H.J. Kim, I.K. Park, H.J. Kang, H.C. Shin, D. Baek, Y. Choi, K.H. Park, W.L. Jin, Effects of structurally stabilized EGF and bFGF on wound healing in type I and type II diabetic mice, Acta Biomater. 66 (2017) 325–334, https://doi.org/10.1016/j.actbio.2017.11.045.

[20] L. Yildirimer, N.T.K. Thanh, A.M. Seifalian, Skin regeneration scaffolds: a multimodal bottom-up approach, Trends Biotechnol. 30 (2012) 638–648, https://doi.org/10.1016/j.tibtech.2012.08.004.

[21] B.A. Stoll, The growth hormone/insulin-like growth factor axis and breast cancer risk, Breast 2 (1993) 130–133, https://doi.org/10.1016/0960-9776(93)90054-J.

[22] Y. Niu, Q. Li, Y. Ding, L. Dong, C. Wang, Engineered delivery strategies for enhanced control of growth factor activities in wound healing, Adv. Drug Deliv. Rev. 146 (2018) 190–208, https://doi.org/10.1016/j.addr.2018.06.002.

[23] Z. Chen, Z. Zhang, J. Feng, Y. Guo, Y. Yu, J. Cui, H. Li, L. Shang, The influence of Mussel-Derived Bioactive BMP-2 decorated PLA on MSCs behavior in vitro and verification with osteogenicity at ectopic sites in vivo, ACS Appl. Mater. Interfaces 10 (2018) 11961–11971, https://doi.org/10.1021/acsami.8b01547.

[24] C. Zhang, H. Miyatake, Y. Wang, T. Inaba, Y. Wang, P. Zhang, Y. Ito, A bioorthogonal approach for the preparation of a titanium-binding insulin-like growth-factor-1 derivative by using tyrosinase, Angew. Chem. 55 (2016) 1447–11451, https://doi.org/10.1002/anie.201603155.

[25] Z. Hong, P. Zhang, A. Liu, L. Chen, X. Chen, X. Jing, Composites of poly(lactide-co-glycolide) and the surface modified carbonated hydroxyapatite nanoparticles, J. Biomed. Mater. Res. A 81A (2010) 515–522, https://doi.org/10.1002/jbm.a.31038.

[26] Y. Myunggu, L. Hyeongjin, K. Geunhyung, Three-dimensional hierarchical composite scaffolds consisting of polycaprolactone, β-tricalcium phosphate, and collagen nanofibers: fabrication, physical properties, and in vitro cell activity for bone tissue regeneration, Biomacromolecules 12 (2011) 502–510, https://doi.org/10.1021/bm1013052.

[27] H. Lee, S.M. Dellatore, W.M. Miller, P.B. Messersmith, Mussel-inspired surface chemistry for multifunctional coatings, Science 318 (2007) 426–430, https://doi.org/10.1126/science.1147241.

[28] X. Rui, G. Luo, H. Xia, W. He, Z. Jian, L. Bo, J. Tan, J. Zhou, D. Liu, Y. Wang, Novel bilayer wound dressing composed of silicone rubber with particular micropores

enhanced wound re-epithelialization and contraction, Biomaterials 40 (2015) 1–11, https://doi.org/10.1016/j.biomaterials.2014.10.077.
[29] Y. Wang, C. Fu, Z. Wu, L. Chen, X. Chen, Y. Wei, P. Zhang, A chitin film containing basic fibroblast growth factor with a chitin-binding domain as wound dressings, Carbohydr. Polym. 174 (2017) 723–730, https://doi.org/10.1016/j.carbpol.2017.05.087.
[30] Z. Wang, L. Chen, Y. Wang, X. Chen, P. Zhang, Improved cell adhesion and osteogenesis of op-HA/PLGA composite by poly(dopamine)-assisted immobilization of collagen mimetic peptide and osteogenic growth peptide, ACS Appl. Mater. Interfaces 8 (2016) 26559–26569, https://doi.org/10.1021/acsami.6b08733.
[31] J. Wu, J. Zhu, C. He, Z. Xiao, J. Ye, Y. Li, A. Chen, H. Zhang, X. Li, L. Lin, Comparative study of heparin-poloxamer hydrogel modified bFGF and aFGF for in vivo wound healing efficiency, ACS Appl. Mater. Interfaces 8 (2016) 18710–18721, https://doi.org/10.1021/acsami.6b06047.
[32] C. Yi, L. Yan, T. Yuan, Q. Zhang, H. Fan, Asymmetric polyurethane membrane with in situ-generated nano-TiO_2 as wound dressing, J. Appl. Polym. Sci. 119 (2010) 1532–1541, https://doi.org/10.1002/app.32813.
[33] N. Zhang, T. Gao, Y. Wang, Z. Wang, P. Zhang, J. Liu, Environmental pH-controlled loading and release of protein on mesoporous hydroxyapatite nanoparticles for bone tissue engineering, Mater. Sci. Eng. C Mater. Biol. Appl. 46 (2015) 158–165, https://doi.org/10.1016/j.msec.2014.10.014.
[34] X. Wang, F. Cheng, J. Liu, J.H. Smått, D. Gepperth, M. Lastusaari, C. Xu, L. Hupa, Biocomposites of copper-containing mesoporous bioactive glass and nanofibrillated cellulose: biocompatibility and angiogenic promotion in chronic wound healing application, Acta Biomater. 46 (2016) 286–298, https://doi.org/10.1016/j.actbio.2016.09.021.
[35] S.M. Pawde, K. Deshmukh, S. Parab, Preparation and characterization of poly(vinyl alcohol) and gelatin blend films, J. Appl. Polym. Sci. 109 (2010) 1328–1337, https://doi.org/10.1002/app.28096.
[36] H. Yılmaz, S.H. Sanlıer, Preparation of magnetic gelatin nanoparticles and investigating the possible use as chemotherapeutic agent, Artif. Cells Nanomed. Biotechnol. 41 (2013) 69–77, https://doi.org/10.3109/21691401.2012.745863.
[37] Y. Huang, N. Dan, W. Dan, W. Zhao, Z. Bai, Y. Chen, C. Yang, Facile fabrication of gelatin and polycaprolactone based bilayered membranes via spin coating method with antibacterial and cyto-compatible properties, Int. J. Biol. Macromol. 124 (2019) 699–707, https://doi.org/10.1016/j.ijbiomac.2018.11.262.
[38] N.C. Carrejo, A.N. Moore, T.L.L. Silva, D.G. Leach, I.C. Li, D.R. Walker, J.D. Hartgerink, Multidomain peptide hydrogel accelerates healing of full-thickness wounds in diabetic mice, ACS Biomater. Sci. Eng. 4 (2018) 1386–1396, https://doi.org/10.1021/acsbiomaterials.8b00031.
[39] G.H. Yang, F. Mun, G.H. Kim, Direct electrospinning writing for producing 3D hybrid constructs consisting of microfibers and macro-struts for tissue engineering, Chem. Eng. J. 288 (2016) 648–658, https://doi.org/10.1016/j.cej.2015.12.047.
[40] Lingzhi Kong, Zhi Wu, Huakun Zhao, Haomin Cui, Ji Shen, Bioactive injectable hydrogels containing desferrioxamine and bioglass for diabetic wound healing, ACS Appl. Mater. Interfaces 10 (2018) 30103–30114, https://doi.org/10.1021/acsami.8b09191.
[41] K. Jong-Woo, S. Kwan-Ha, K. Young-Hag, H.M. Jin, M. Jiyoung, K. Hyoun-Ee, Production of poly(ε-caprolactone)/hydroxyapatite composite scaffolds with a tailored macro/micro-porous structure, high mechanical properties, and excellent bioactivity, Materials 10 (2017) 1123, https://doi.org/10.3390/ma10101123.
[42] G. Colon, B.C. Ward, T.J. Webster, Increased osteoblast and decreased Staphylococcus epidermidis functions on nanophase ZnO and TiO_2, J. Biomed. Mater. Res. A 78A (2010) 595–604, https://doi.org/10.1002/jbm.a.30789.
[43] L. Zeng, Y. Yao, D.A. Wang, X. Chen, Effect of microcavitary alginate hydrogel with different pore sizes on chondrocyte culture for cartilage tissue engineering, Mater. Sci. Eng. C 34 (2014) 168–175, https://doi.org/10.1016/j.msec.2013.09.003.
[44] X. Le, G.E.J. Poinern, N. Ali, C.M. Berry, D. Fawcett, Engineering a biocompatible scaffold with either micrometre or nanometre scale surface topography for promoting protein adsorption and cellular response, Int. J. Biomater. 2013 (2013) 1–16, https://doi.org/10.1155/2013/782549.
[45] C.Y. Chien, W.B. Tsai, Poly(dopamine)-assisted immobilization of Arg-Gly-Asp peptides, hydroxyapatite, and bone morphogenic protein-2 on titanium to improve the osteogenesis of bone marrow stem cells, ACS Appl. Mater. Interfaces 5 (2013) 6975–6983, https://doi.org/10.1021/am401071f.
[46] L. Soung-Hoon, Z. Muhammad, H. Jae-Kwan, M. Do Sik, C. Kang-Yell, Valproic acid induces cutaneous wound healing in vivo and enhances keratinocyte motility, PLoS One 7 (2012) e48791, , https://doi.org/10.1371/journal.pone.0048791.
[47] M.T. Cerqueira, L.P. da Silva, T.C. Santos, R.P. Pirraco, V.M. Correlo, R.L. Reis, A.P. Marques, Gellan gum-hyaluronic acid spongy-like hydrogels and cells from adipose tissue synergize promoting neoskin vascularization, ACS Appl. Mater. Interfaces 6 (2014) 19668–19679, https://doi.org/10.1021/am504520j.
[48] S. Selvaraj, N.N. Fathima, Fenugreek incorporated silk fibroin nanofibers—a potential antioxidant scaffold for enhanced wound healing, ACS Appl. Mater. Interfaces 9 (2017) 5916–5926, https://doi.org/10.1021/acsami.6b16306.
[49] X. Wang, J. Ge, E.E. Tredget, Y. Wu, The mouse excisional wound splinting model, including applications for stem cell transplantation, Nat. Protoc. 8 (2013) 302–309, https://doi.org/10.1038/nprot.2013.002.